Article

A Coherent Integration Segment Searching Based GRT-GRFT Hybrid Integration Method for Arbitrary Fluctuating Target

Zhenghe Zhang [ID], Nan Liu *, Yongning Hou, Shiyu Zhang and Linrang Zhang

National Laboratory of Radar Signal Processing, Xidian University, Xi'an 710071, China; zhangzhenghe@stu.xidian.edu.cn (Z.Z.); 20021210894@stu.xidian.edu.cn (Y.H.); zhangshiyu@stu.xidian.edu.cn (S.Z.); lrzhang@xidian.edu.cn (L.Z.)
* Correspondence: n_liu@mail.xidian.edu.cn

Abstract: Long-time integration is an effective method for improving the signal–to–noise ratio (SNR) of an echo. However, if the target radar cross-section (RCS) fluctuates over the long integration time, the traditional coherent integration and noncoherent integration methods will produce significant performance losses, making it impossible to achieve a favorable integration performance at low SNRs. This study proposes a new hybrid integration method based on the generalized Radon–Fourier transform (GRFT) and generalized Radon transform (GRT) for targets with which echoes are partially coherent. First, a coherent integration is performed with GRFT within the optimal coherent processing segment using optimal coherent processing segmented matching. Then, the GRT is used for noncoherent integration between the coherent processing sections, and the target motion parameters are obtained through a global search. Compared with the GRFT, GRT, and moving target detection (MTD)-GRT methods, the proposed method applies to targets with arbitrary RCS fluctuations, arbitrary cross-range cells, and cross-Doppler cells, and offers the best detection performance. Finally, both simulation results and measured data processing results demonstrate the effectiveness of the algorithm.

Keywords: hybrid integration; generalized Radon-Fourier transform (GRFT); generalized Radon transform (GRT); arbitrary fluctuating target

1. Introduction

At present, dim target detection requires long-time integration to improve the signal-to-noise ratio (SNR) of the echo due to the low SNR of the single pulse echo of the target [1–3]. Moreover, during radar illumination, both coherent integration algorithms and noncoherent integration methods can result in significant performance losses. Such losses can also occur due to the development of cross-range cells and cross-Doppler cells caused by either the high-speed maneuvering of the targets or high radar resolutions [4–6] and because the motion of the target relative to the radar causes the target radar cross-section (RCS) to fluctuate, which brings about partial correlation of the target echo [7–12]. At this point, the coherent-noncoherent hybrid integration method helps avoid significant degradation of the coherent integration's performance in the areas with a weak echo correlation along with the problem of SNR thresholds regarding noncoherent integration. The coherent processing time is matched with the decorrelation time of the target echo to achieve better integration performance [13,14], which has become a research topic of considerable interest in recent years.

The current long-time integration methods can be classified into noncoherent integration [15–24], coherent integration [25–43], and coherent-noncoherent hybrid integration [44–48]. Since these methods were easy to implement, the early-stage algorithms were largely noncoherent integration algorithms. Typical noncoherent integration methods include projection transformation algorithms [15–18], dynamic programming algorithms [19–22], and particle

filter algorithms [23,24]. These methods are effective for echoes with high SNRs, but they do not work for echoes with low SNRs. In addition, the coherent integration algorithms can achieve considerable integration gain at low SNRs, since they take full advantage of the phase information of the echo; hence, they have been extensively studied. The coherent integration algorithms can be divided into four categories based on their applicable target motion models: uniform motion algorithms [25–30], uniformly accelerated motion algorithms [31–33], uniform jerk motion algorithms [34–36], and high-order complex motion algorithms [37–40]. In addition, there are some compressive sensing algorithms [41–43] once the Nyquist sampling rate cannot be satisfied. The above algorithms are all operating under the assumption that the target echoes are completely correlated within the time period of the integration. In many cases, however, due to the long time spanning of the echo integration, the attitude change of the target relative to the radar results in partial echo correlation, ranging between completely correlated and completely uncorrelated. Not all phase information has a positive effect on integration, which consequently demonstrates the fact that the coherent integration of phase information cannot solely bring favorable integration effects. In such cases, hybrid integration is an effective approach for solving this problem. Jiankui Zeng et al. divided the whole observation time into several coherent processing segments under the condition that there is no range migration [45]. In each coherent processing segment, the moving target detection (MTD) method was used for coherent integration, and then the Hough transform was used for noncoherent integration between segments. In Reference [46], the MTD method was also used for the coherent integration in coherent processing segments, while the generalized Radon transform (GRT) was employed for noncoherent integration between segments. All the hybrid integration algorithms require that there should be no range migration in each coherent processing segment, which leads to a short coherent integration time for high-speed targets or radar signals with a high resolution. Since there are only few pulses in the coherent integration time period, it is impossible to fully play to the high coherent integration gain. Therefore, it is necessary to further increase the length of the coherent integration segment. The improved MTD-GRT algorithm in Reference [47] can sufficiently increase the segment length of coherent integration, although the method requires prior information to compensate for the target motion, which is difficult to obtain with unknown targets. Reference [48] principally studied the hybrid integration detector and the optimal number of coherent integration pulses. The segment length of coherent integration is dependent on the covariance matrix of the echo, so it is difficult to obtain such information in the case of low SNRs.

In this study, a new hybrid integration algorithm for cross-range cell and cross-Doppler cell targets in RCS fluctuation and integration time is proposed. Firstly, optimal coherent processing segmented matching is used for coherent integration through the generalized Radon-Fourier transform (GRFT) algorithm within the coherent integration segment. Then, the GRT method is employed for noncoherent integration. The simulation test results demonstrate the effectiveness of the proposed algorithm.

The rest of the article is organized as follows: Section 2 describes the signal model and the current problems; the overall procedure of the hybrid integration detection algorithm and the coherent integration segmented matching algorithm are presented in Section 3; in Section 4, the simulation test results and the measured data processing results are given; and finally, the whole study is summarized and conclusions are drawn in Section 5. These sections should define the purpose of the work and its significance.

2. Signal Model and Problem Analysis

Assuming that the radar emits linear frequency modulation (LFM) pulses, a high-speed and highly maneuverable target can be regarded as a point target, and pulse compression of the echo signals leads to:

$$s(n,m) = \sigma(m) sinc\left(n - \frac{R(m)}{\rho_r}\right) \exp\left[-j\frac{4\pi}{\lambda}R(m)\right] + N(n,m) \tag{1}$$

where m and n are the slow-time sampling point number and the in-pulse fast-time sampling point number, respectively. $\rho_r = c/2B$ denotes the range resolution. c represents the speed of light. B is the signal bandwidth. $\lambda = c/f_c$ stands for the wavelength; $sinc(\cdot)$ is the sinc function, where $sinc(x) = \frac{\sin(x)}{x}$. T_r is the radar pulse repetition cycle and R denotes the radial range of the target. Here, consider a target in uniformly accelerated motion, whose radial range can be expressed as $R(m) = r_0 + vmT_r + 1/2a(mT_r)^2$, where r_0 represents the initial range, v is the initial velocity, and a is the acceleration. σ is the complex backscattering coefficient of the echo for the target at different times, and N denotes noise. Due to the high speed and the strong maneuverability of the target, echo decorrelation occurs during radar illumination. Here, the relief target model is considered to obey the Gaussian distribution.

Its correlation function is as follows:

$$R_\sigma(m) = \frac{1}{\sqrt{2\pi}T_{CI}} \exp\left(-\frac{mT_r^2}{2T_{CI}^2}\right) \qquad (2)$$

where T_{CI} represents the echo decorrelation time.

According to the signal envelope resulting from pulse compression in (1), range migration causes the signal envelope peak position $sinc\left\{n - \frac{R(m)}{\rho_r}\right\}$ to vary in every pulse, resulting in a performance loss due to integration. For the Doppler phase term $\exp\left[-j\frac{4\pi R(m)}{\lambda}\right]$ in (1), when the velocity of the target is substantial, cross-Doppler cells develop, which may also bring about integration performance loss. Therefore, the above issues cannot be ignored for integration algorithm design.

Where the SNR is at a low level after pulse compression, it is a common practice to improve the target detection performance of radar through pulse integration. Assuming that K pulses are integrated, range migration compensation and Doppler phase compensation should be performed before integration. The coherent integration process can be summarized as follows:

$$\begin{aligned} y_{CI} &= \sum_{i=1}^{K} [s(n,i)h(i) + N(n,i)] \\ &= \sum_{i=1}^{K} [\sigma(i)s_p(n,i)h(i) + N(n,i)] \end{aligned} \qquad (3)$$

where $s_p(n,i) = sinc\left(n - \frac{R(i)}{\rho_r}\right)\exp\left[-j\frac{4\pi}{\lambda}R(i)\right]$, y_{CI} is the coherent integration result; h represents the phase compensation function, while $|h(i)| = 1$ depending on the compensation method, different phase compensation functions may appear; and the phase compensation function is discussed in subsequent sections of the present study.

The signal power after integration is calculated as:

$$\begin{aligned} \sigma_S^2 &= \mathrm{E}\left[\left(\sum_{i=1}^{K} \sigma(i)s_p\left(\frac{R(i)}{\rho_r}, i\right)h(i)\right)\left(\sum_{l=1}^{K} \sigma(l)s_p\left(\frac{R(l)}{\rho_r}, l\right)h(l)\right)^*\right] \\ &= \sum_{i=1}^{K}\sum_{l=1}^{K} \chi\left(\frac{R(i)}{\rho_r} - \frac{R(l)}{\rho_r}\right)\mathrm{E}[\sigma(i)\sigma^*(l)] \end{aligned} \qquad (4)$$

where $\chi(\cdot)$ is the ambiguity function of the LFM signal; the best integration result can be achieved through range migration compensation that is, when $i = l$, the compensation for

the range migration is finished; when $i = l$, i.e., upon completion of the compensation task, $\chi\left(\frac{R(i)}{\rho_r} - \frac{R(l)}{\rho_r}\right) = \sigma_{S_p}^2$, $E[\sigma(i)\sigma^*(l)] = \delta^2$; then, (4) can be further expressed as:

$$
\begin{aligned}
\sigma_S^2 &= \sigma_{S_p}^2 \cdot E\left[\left(\sum_{i=1}^{K}\sigma(i)\right)\left(\sum_{l=1}^{K}\sigma(l)\right)^*\right] \\
&= \sigma_{S_p}^2 \cdot \left(K\delta^2 + \sum_{i\neq l}\sigma(i)\sigma^*(l)\right) \\
&= \sigma_{S_p}^2 \cdot \delta^2\left(K + 2\sum_{i=1,}^{K-1}\sum_{j=1,i\neq j}^{K-1}R_\sigma(|i-j|)\right)
\end{aligned}
\tag{5}
$$

The post-integration noise power is:

$$
\begin{aligned}
\sigma_N^2 &= \sum_{i,l=1}^{K} E[N(n,i)N^*(n,l)] \\
&= K\sigma_{ny}^2
\end{aligned}
\tag{6}
$$

where σ_{ny}^2 is the noise power in individual pulses. The post-coherent integration SNR can be expressed as:

$$
SNR_{CI} = \frac{\sigma_S^2}{\sigma_N^2} = \frac{\sigma_{S_p}^2 \cdot \delta^2\left(K + 2\sum\limits_{i=1,}^{K-1}\sum\limits_{j=1,i\neq j}^{K-1}R_\sigma(|i-j|)\right)}{K\sigma_{ny}^2}
\tag{7}
$$

When the echo is completely correlated, it is reasonable that $R_\sigma(i) = 1$. According to (7), the SNR of the coherent integration increases **K** times at this point. Where the echo is completely unrelated, it is reasonable that $R_\sigma(i) = 0$. If coherent integration is employed at this point, there would be no SNR improvement. Where the echo is partially coherent, the improved SNR after coherent integration is associated with the echo decorrelation time. With the growth of the coherent integration segment, the gain from coherent integration grows slowly because the echo correlation becomes weak, while the noise power increases linearly with the increase in the number of integration pulses. In the areas with weak echo correlation, the rate at which signal power integration increases is decreased; as a result, the SNR is improved by a smaller margin.

In contrast, noncoherent integration removes the phase information from the echo, and the objects of the integration are normally the amplitude of post-pulse compression data or its square. In this study, the square of the signal after pulse compression is used for integration, which can be expressed as:

$$
y_{NCI} = \sum_{i=1}^{K}\left|\sigma(i)s_A\left(\frac{viT_r + 1/2a(iT_r)^2}{\rho_r}, i\right) + N(n,i)\right|^2
\tag{8}
$$

where $s_A = sinc\left(n - n_0 - \frac{viT_r + 1/2a(iT_r)^2}{\rho_r}\right)$.

Noncoherent integration is a nonlinear process, in which the SNR is improved by $K \sim \sqrt{K}$ times theoretically. With the increase in the number of integration pulses, the SNR improvement gain of noncoherent integration progressively decays to $\sqrt{K}$ times, theoretically [49], and the effect will suffer a major setback when coherent integration is further used for processing. As shown in Figure 1, in contrast to the case in which the integration pulse count is proportional to the integration gain when the echo is completely correlated, the maximum coherent integration gain cannot be achieved through the coherence of all pulses, whereas integration is performed for a partially coherent target echo. The maximum integration gain is impossible to achieve without matching the integration time with the echo decorrelation time.
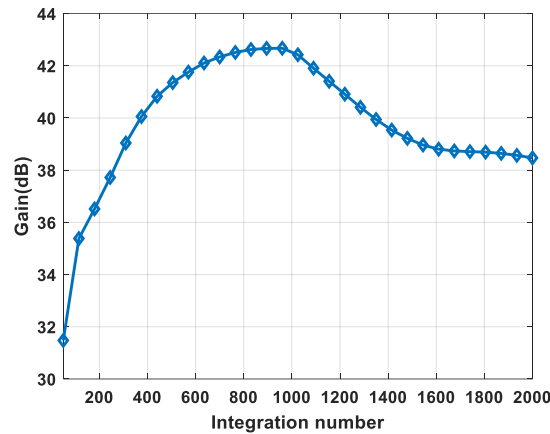
Figure 1. Coherent integration performance for partially coherent echo.

Therefore, to maximize the integration gain during integration for a target that is partially coherent with the echo, the coherent-noncoherent hybrid integration approach should be employed, as shown in Figure 2. In this approach, the whole integration time is divided into several coherent integration segments, within which coherent integration is adopted in coherent integration segments while the noncoherent integration method is employed to reintegrate the energy within the coherent integration segments. Thus, by combining both integration methods, the echo SNR is improved to the greatest extent.
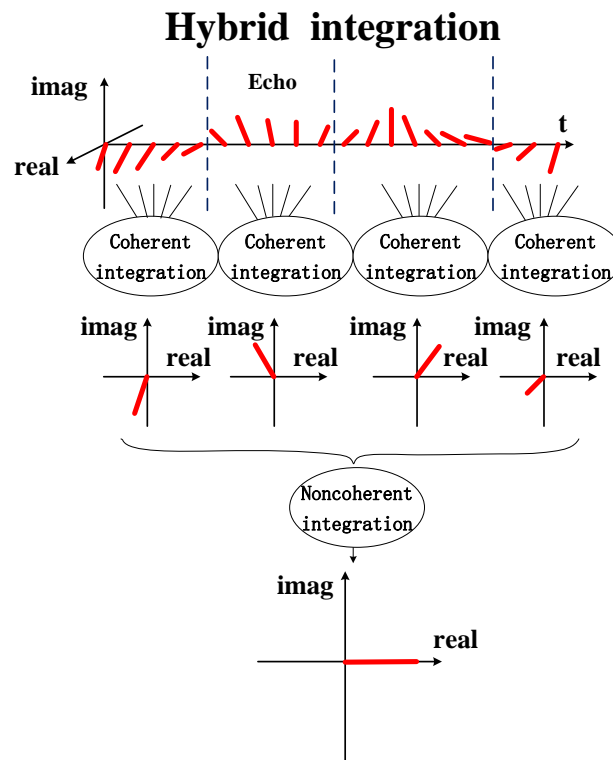

Figure 2. Hybrid integration for partially coherent echo.

3. Hybrid Integration Detection Algorithm

Where the echo is partially coherent, the hybrid integration algorithm offers optimal detection performance. Therefore, it is necessary to study the hybrid integration algorithm. This part of the study is divided into two parts: the compensation approach for range migration and Doppler migration resulting from high-speed target maneuvering, and the matching used for the optimal coherent integration segmentation.

Since the echo data are partially coherent, the entire echo should first be divided into several coherent processing segments. The coherent processing segmentation time should theoretically be close to the decorrelation time of the echo signal, allowing the maximum integration gain to be achieved by coherent processing at this point. The matching of the coherent processing segments is discussed in detail in a later part of this section.

The GRFT is used for coherent integration. Assuming that the total integration time is divided into K_{CI} coherent integration segments, the number of pulses in each segment can be expressed as:

$$k_{CI} = K/K_{CI} \tag{9}$$

The phase compensation function within the *i*-th coherent integration segment can be expressed as:

$$h_i(m) = \exp\left(j4\pi \cdot \frac{R_{search}(p,q,i,l,k_{CI})}{\lambda}\right) \tag{10}$$

where
$$\begin{aligned} R_{search}(p,q,i,l,k_{CI}) &= v(p) \cdot ((i-1)k_{CI}T_r + mT_r) \\ &+ \tfrac{1}{2}a(q) \cdot ((i-1)k_{CI}T_r + mT_r)^2. \end{aligned}$$

Then, the result of coherent integration in the *i*-th coherent integration segment can be expressed as:

$$g_{CI}(o,p,q,i) = \sum_{l=1}^{k_{CI}} s\left(n, \frac{r(o) + R_{search}(p,q,i,l,k_{CI})}{\rho_r}\right) \cdot h_i(l) \tag{11}$$

where $r(o)$, $v(p)$, and $a(q)$ represent the search range, velocity, and acceleration parameters, respectively. This is just an example of a uniform acceleration model; in essence, the coherent integration method of the GRFT is applicable to the coherent integration of targets with arbitrary high-order motion parameters. The data after pulse compression are a under 2D-time domain at first, and after this step, they have been transformed into motion parameter space.

At this point, the search for motion parameters enables an independent coherent integration process. However, provided that it is often impossible to detect the target within a coherent integration segment due to the low echo SNR of dim targets, it is also necessary to perform coherent integration for each coherent integration segment and to perform noncoherent integration for the integration result of the coherent integration segment before the result of the hybrid integration process can be obtained. Next, the GRT is used to perform noncoherent integration between coherent integration segments to further improve the integration gain. The final integration result is as follows:

$$g_{HI}(o,p,q) = \sum_{i=1}^{K_{CI}} \left| \sum_{l=1}^{k_{CI}} s\left(n, \frac{r(o) + R_{search}(p,q,i,l,k_{CI})}{\rho_r}\right) \cdot h_i(l) \right|^2 \tag{12}$$

Next, all search cells should be traversed, and the presence or absence of the targets in each search cell should be judged using the following equation:

$$g_{HI}(o,p,q) \underset{H_0}{\overset{H_1}{\gtrless}} V_T \tag{13}$$

where V_T is the detection threshold. H1 and H0 represent the hypothetical cases in which noise and target information coexist and only noise is present, respectively. A detailed derivation is provided in Appendix A.

Figure 3 adequately describes the process used for this algorithm: first, all the echo data are divided into several coherent integration segments in time, and coherent integration is performed in the range-velocity domain. Then, noncoherent integration is performed along the target trajectory to yield the final hybrid integration result.
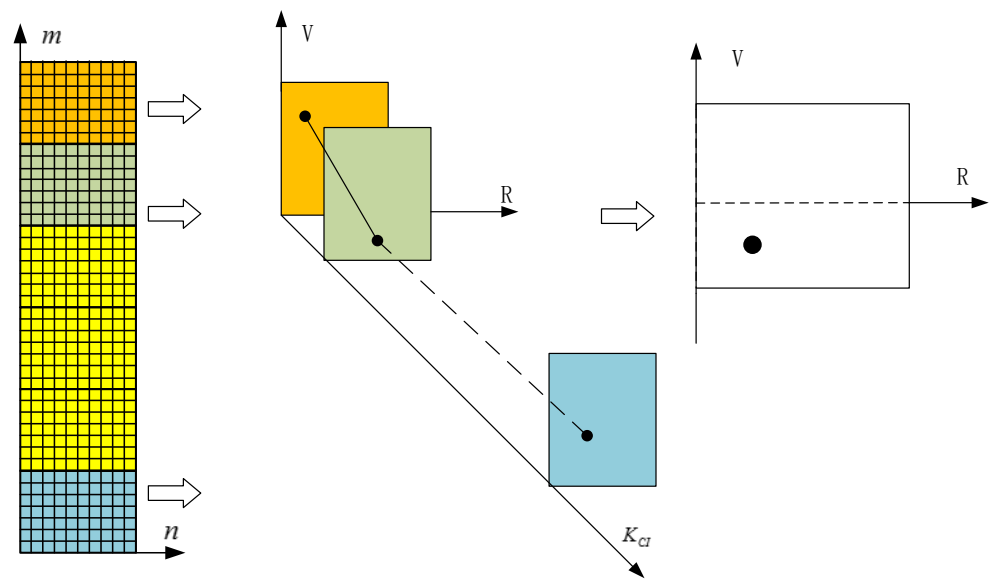
Figure 3. Diagrammatic drawing for hybrid integration.

According to Figure 1, since the target echo is partially coherent, the selection of coherent integration segments may affect the integration gain of the echo. When the coherent integration segment length matches the echo signal correlation time, the maximum integration gain can be achieved. Theoretically, as long as the decorrelation time of the echo is yielded, the coherent integration segment length in the hybrid integration can be determined based on the echo decorrelation time. However, in practice, the echo correlation of a dim target is unpredictable, so this study proposes an optimal coherent integration segment matching search algorithm. The algorithm consists of two steps, as shown in Figure 4. First, the number of pulses in the coherent integration segment can be expressed as $k_{CI} = [1, 2, \cdots, K]$; obviously, the number of pulses, k_{CI}, in the coherent integration segment should be a positive integer. The corresponding number of coherent integration segments can be expressed as:

$$K_{CI}(w) = \lceil K/k_{CI}(w) \rceil \tag{14}$$

where $\lceil \cdot \rceil$ denotes the "round-up-to-integer" operation.

Then, different coherent integration segments are subjected to coherent integration; for different coherent integration segments, the phase compensation function within the i-th coherent integration segment can be expressed as:

$$h_i(m, w) = \exp\left(j4\pi \cdot \frac{R_{search}(p, q, i, l, k_{CI}(w))}{\lambda} \right) \tag{15}$$

where $\begin{aligned} R_{search}(p, q, i, l, k_{CI}(w)) &= v(p) \cdot ((i-1)k_{CI}(w)T_r + mT_r) \\ &\quad + \tfrac{1}{2}a(q) \cdot ((i-1)k_{CI}(w)T_r + mT_r)^2 \cdot \end{aligned}$

Furthermore, the result of coherent integration in different coherent integration segments can be expressed as:

$$g_{CI}(o, p, q, i, w) = \sum_{l=1}^{k_{CI}(w)} s\left(n, \frac{r(o) + R_{search}(p, q, i, l, k_{CI}(w))}{\rho_r} \right) \cdot h_i(l, w) \tag{16}$$

The final hybrid integration result under different coherent integration segments can be expressed as:

$$g_{HI}(o,p,q,w) = \sum_{i=1}^{K_{CI}(w)} \left| \sum_{l=1}^{k_{CI}(w)} s\left(n, \frac{r(o) + R_{search}(p,q,i,l,k_{CI}(w))}{\rho_r} \right) \cdot h_i(l,w) \right|^2 \tag{17}$$

For optimal hybrid coherent integration detection under coherent conditions of the target echo portion, each possible coherent time should be taken as a parameter and searched to ensure that it can be matched with an optimal coherent processing segment. This fact, combined with the search for target motion parameters in prior hybrid integration activities, may necessitate an immense computing load. Therefore, fast algorithms must be studied. To reduce the number of match searches, the echo sequence can be segmented by the segment length corresponding to the minimum coherent time of the echo, which is denoted as $t_{\min}$. Based on current radar processing capabilities, either four or eight pulses are normally selected as the minimum coherent integration segments. At this point, the number of pulses in the coherent integration segment is $k_{\min} = t_{\min}/T_r$, and the total number of coherent integration segments is $K_{\min} = K/k_{\min}$; the echo data in the segments are subjected to coherent integration. Thus, the compensation function in the i-th coherent integration segment can be expressed as:

$$h_{\min}(i,m) = \exp\left(j4\pi \cdot \frac{R_{search}(p,q,i,l,k_{\min})}{\lambda} \right) \tag{18}$$

where
$$R_{search}(p,q,i,l,k_{\min}) = ((i-1)k_{\min}T_r + lT_r)v(p) \\ +1/2((i-1)k_{\min}T_r + lT_r)^2 a(q).$$

Then, the coherent integration result can be expressed as:

$$g_{CI}^{(1)}(o,p,q,l) = \sum_{l=1}^{k_{\min}} s\left(n, \frac{r(o) + R_{search}(p,q,i,l,k_{\min})}{\rho_r} \right) \cdot h_{\min}(i,l) \tag{19}$$

In this way, the minimum coherent integration output data are constructed. The output data of the two adjacent segments are once more subjected to coherent integration to form the output data of the next level of coherent integration, that is:

$$g_{CI}^{(2)}(o,p,q,l) = g_{CI}^{(1)}(o,p,q,2(l-1)+1) + g_{CI}^{(1)}(o,p,q,2l) \tag{20}$$

It should be noted that the coherent integration time becomes $2t_{\min}$, while the total number of coherent integration segments correspondingly decreases to $K_2 = K/2k_{\min}$.

Then, the hybrid integration output of this level can be expressed as:

$$g_{HI}^{(2)}(o,p,q) = \sum_{i=1}^{K_2} \left| g_{CI}^{(2)}(o,p,q,i) \right|^2 \tag{21}$$

Similarly, two adjacent data in the next level of data are subjected to coherent integration to form the level-3 coherent integration output data. As shown in Figure 5, the operation above is repeated until the echo coherent time corresponding to the data of this level reaches the maximum coherent time. It should be noted that some segment lengths will be missed due to the fixed rate of segment length increase if the segments are merged pairwise. Thus, it is advisable to change the rate of the segment length increase in coherent integration, to cover as many segments as possible. If possible, it is advisable to use three smaller segments to form the data at the next level for coherent integration:

$$g_{CI}^{(2)}(o,p,q,l) = g_{CI}^{(1)}(o,p,q,3(l-1)+1) + g_{CI}^{(1)}(o,p,q,3(l-1)+2) \\ + g_{CI}^{(1)}(o,p,q,3l) \tag{22}$$
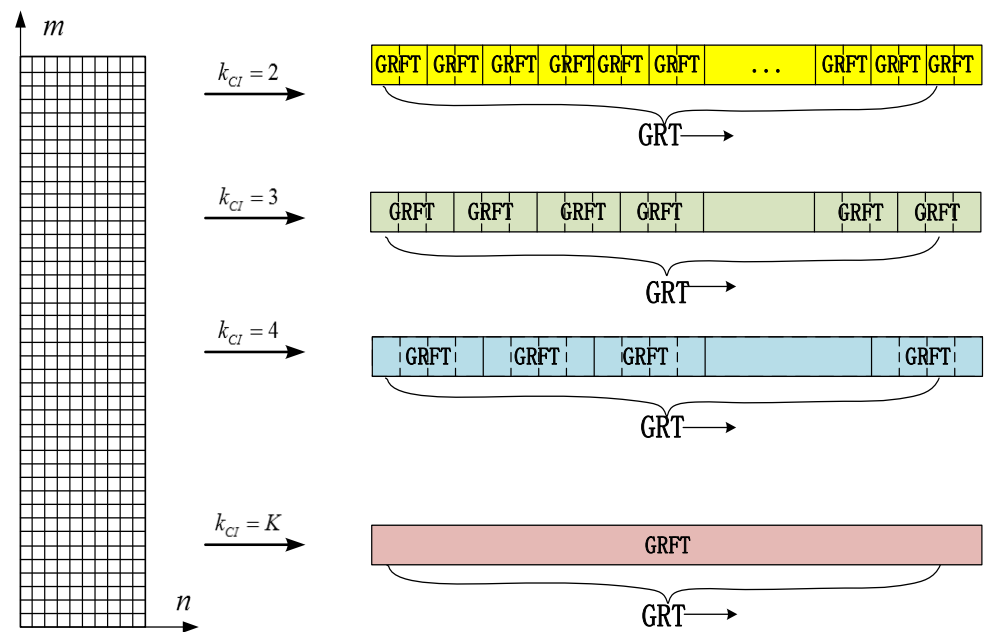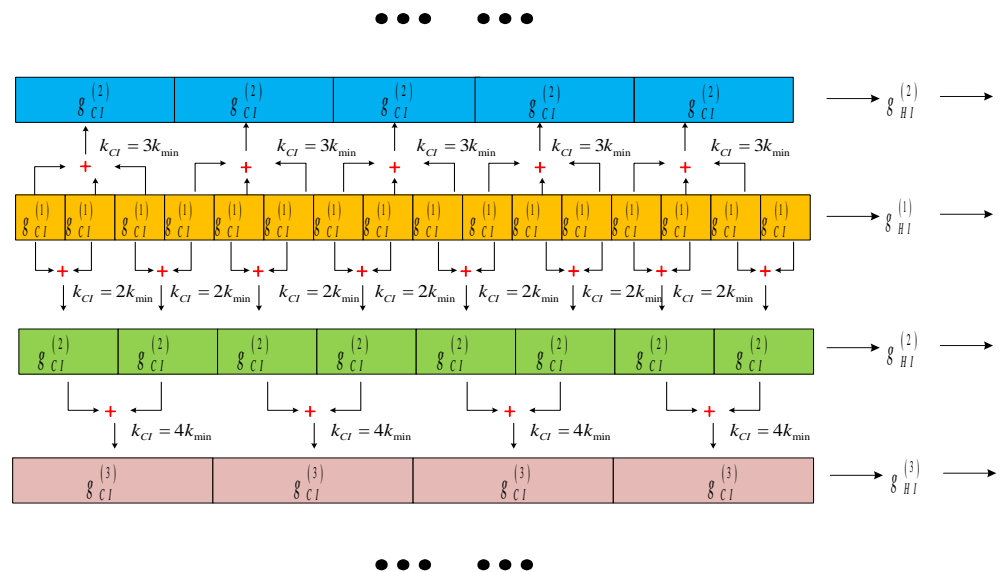
Figure 4. Flowchart of the algorithm.

Figure 5. Diagrammatic drawing for coherent integration segments combination.

At this point, the time for coherent integration becomes $3t_{\min}$, while the total number of coherent integration segments decreases to $K_3 = K/3k_{\min}$. Furthermore, the coherent integration result within coherent integration segments is subjected to noncoherent integration to yield the hybrid integration result of this level.

In this way, the original multiple hybrid integrations can be replaced by simply continually merging the coherent integration results in the segmentation mode corresponding to the minimum coherent time, thereby favorably reducing the computational burden.

4. Simulation Results and Discussion

In this section, several simulation experiments are designed, and the simulation results are presented to verify the effectiveness of the proposed algorithm. The radar simulation parameters used in the simulation are shown in Table 1.

Table 1. Main parameters of the radar.

Parameters	Value
Carrier frequency (f_c)	3 GHz
Sampling frequency (f_s)	20 MHz
Bandwidth (B)	10 MHz
Pulse width (T_p)	51 μs
PRT (T_r)	1 ms
Pulse number (N)	1024
Integration time (T_{HI})	1.024 s
The SNR of the individual pulses	−20 dB

4.1. Comparison of the Individual Target Integration Results

To facilitate the comparison of various algorithms in this experiment, the motion of the target is set to a uniformly low-speed motion and then a uniformly accelerated motion; the motion parameters are shown in Table 2. The decorrelation time for the echo is $t_{CI} = 0.128$ s. The SNR of the individual pulses of the echo is $SNR = -20$ dB. Figures 6 and 7 display the integration simulation results of the coherent integration algorithm GRFT, the noncoherent integration algorithm GRT, the hybrid integration algorithm MTD-GRT, and the proposed algorithm for the two modes of motion. Figures 6a and 7a present the noncoherent integration results in three modes of motion; due to the low echo SNR, it is difficult to clearly identify the integration spikes from both figures. Figures 6b and 7b show the results of coherent integration in two modes of motion; according to the general cognition, the coherent integration incorporating all the phase information of the echo usually yields the optimal integration gain, but the prior condition that must be met is that the echo signal is completely correlated. Where the echo signal is only partially coherent, the phase is not entirely beneficial to the integration process; as a result, the integration result is not satisfactory when the whole echo is subjected to coherent integration processing. Figure 6c,d and Figure 7c,d compare the hybrid integration MTD-GRT and the proposed algorithm integration result in two modes of motion, respectively. According to Figure 5, the initial coherent integration segment is set to $t_{min} = 0.008$ s; that is, $k_{min} = 8$. After iterating four times, the system gets the optimal output. The coherent integration segment of the MTD-GRT method is 0.128 s, which is the same as the echo decorrelation time. As shown in the figures, since a cross-range cell situation is not observed within the coherent integration segment for the target during constant low-speed motion, both the MTD-GRT algorithm and the proposed algorithm can integrate the echo signal well. Where the high-speed motion of the target causes a cross-range cell situation to develop and the maneuverability of the target brings about the cross-Doppler cell situation, the integration gain of the MTD-GRT method decreases sharply, although the proposed algorithm can still yield a favorable integration gain. Figures 6e and 7e present the detection probability curves of the target in two motion modes, respectively, after 1000 Monte Carlo simulations, where the false alarm probability is set to 10^{-6}, and while the SNR interval after pulse compression is set to −18 to 20 dB. It is evident that neither coherent integration nor noncoherent integration offers a favorable detection probability where the echo is partially coherent, while the hybrid integration is approximately 8 dB greater than the coherent integration and noncoherent integration. Furthermore, when the target involves complex motions in the time period of coherent integration, the detection performance of the MTD-GRT method decreases, whereas the proposed method can still offer satisfactory detection performance.

Table 2. Targets motion parameters in different cases.

	Case 1	Case 2
Initial range (R_0)	800 km	800 km
Initial velocity (v)	60 m/s	3400 m/s
Acceleration	0 m/s^2	−10 m/s^2

(**a**)　　　　　　　　　　　　　　　　　　　　　　　(**b**)

(**c**)　　　　　　　　　　　　　　　　　　　　　　　(**d**)

(**e**)

Figure 6. Simulation results in case 1. (**a**) Integration result via GRT; (**b**) Integration result via GRFT; (**c**) Integration result via the proposed method; (**d**) Integration result via MTD-GRT [47]; (**e**) Detection performance for four integration methods [47].

(**a**)

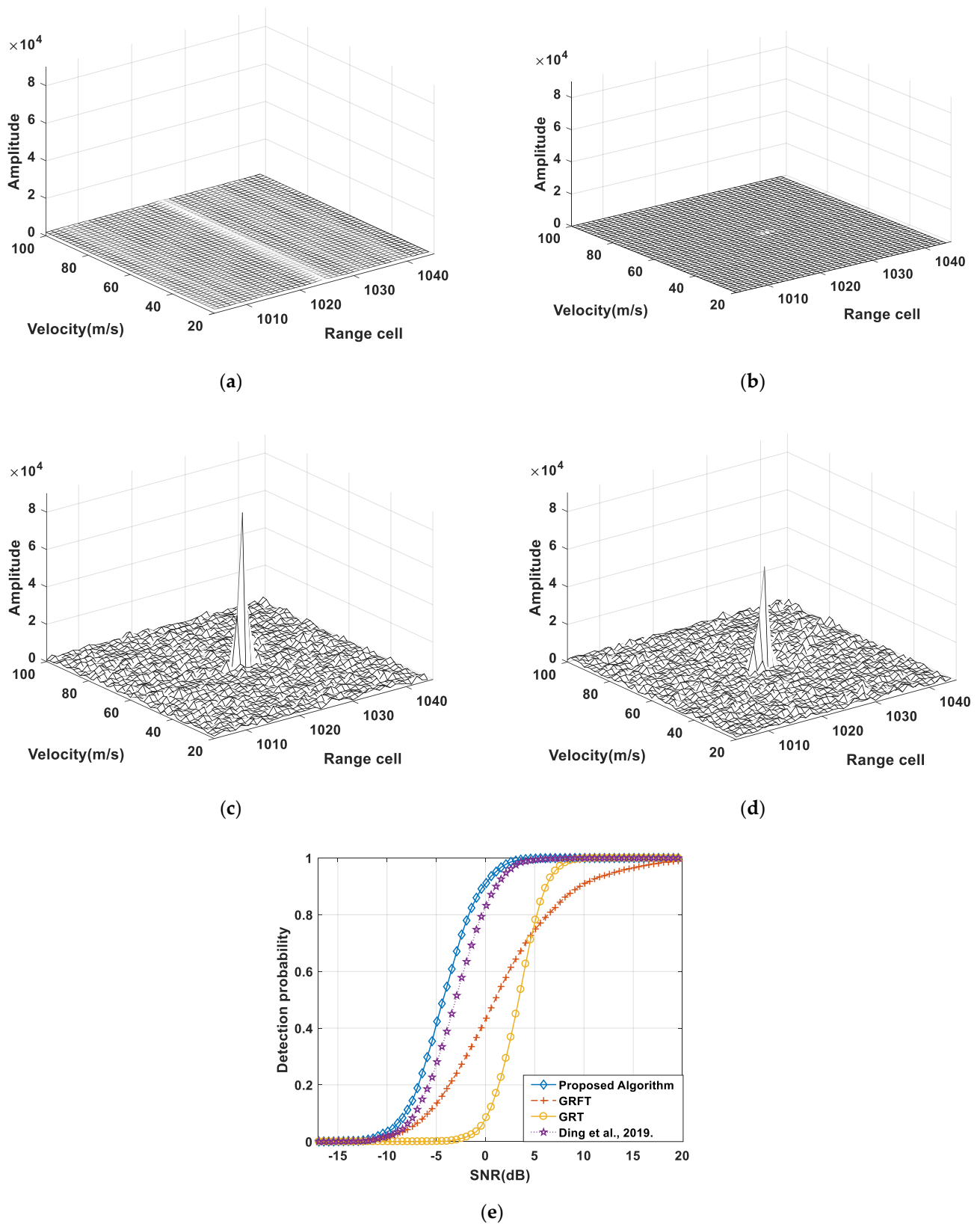
(**b**)

(**c**)

(**d**)

(**e**)

Figure 7. Simulation results in case 2. (**a**) Integration result via GRT; (**b**) Integration result via GRFT; (**c**) Integration result via the proposed method; (**d**) Integration result via MTD-GRT [47]; (**e**) Detection performance for four integration methods [47].
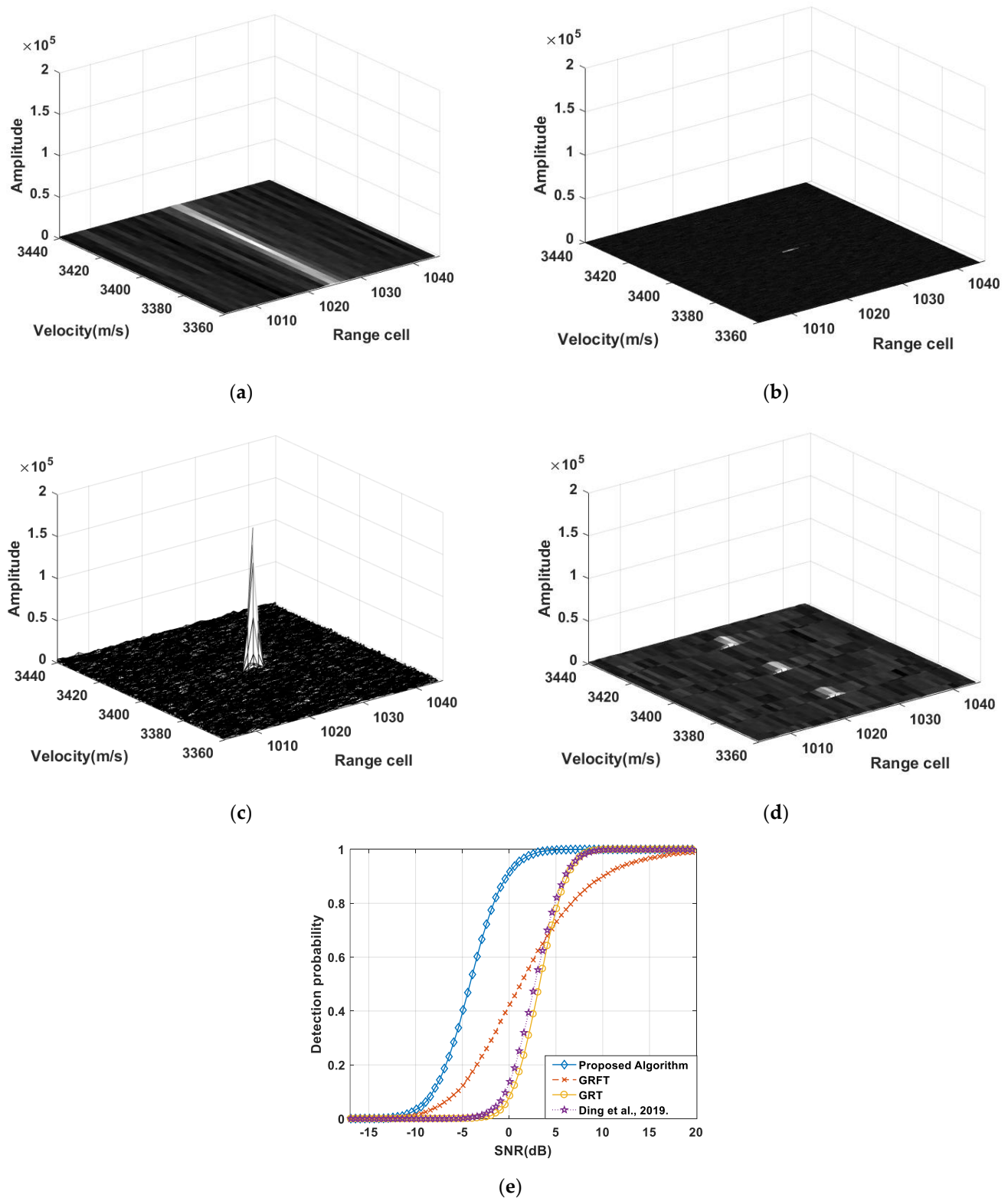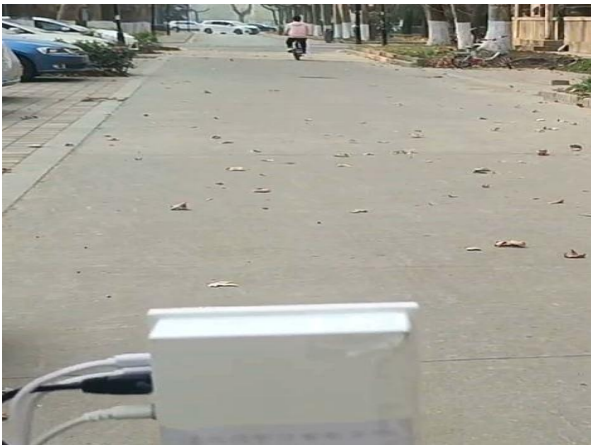
4.2. Processing of the Measured Data

In this experiment, a set of echo data acquired through frequency-modulated continuous-wave radar is processed to verify the effectiveness of the proposed algorithm. The radar

parameters are shown in Table 3; according to the radar parameters, the radar is high resolution. The absolute speed of the target motion is not high during the long-time integration, but compared with the high-resolution radar, both the cross-range cell situation and cross-Doppler cell situation still occur. Furthermore, when the pedestrian moves tangentially relative to the radar, the observation angle of the radar changes greatly in a short period of time, which may lead to a situation in which the echo is partially coherent. For partially coherent target echoes, hybrid integration can theoretically achieve optimal integration detection performance.

Table 3. Main parameters of the FMCW radar.

| Parameters	Value
Carrier frequency (f_c)	77 GHz
Sampling frequency (f_s)	10 MHz
Bandwidth (B)	800 MHz
Modulation time (T_r)	320 μs
Integration time (T_{HI})	2.4576 s

The detection scenario is shown in Figure 8a, where the target is a man raiding an electric bicycle moving tangentially relative to the radar. Since the position relative to the radar changes dramatically in a short period of time, it may lead to a partial correlation with the echo. His initial radial velocity is about 3 m/s; and the initial radial range is about 12 m. It is almost 40 range cells that the target has crossed although the radial velocity is apparently small. The echo data acquired through frequency-modulated continuous-wave radar is a kind of beat signal. The result after FFT is shown in Figure 8b. This operation is equivalent to pulse compression. The data have been transformed to a beat frequency domain. After this step, the target position cannot be seen in the graph, so it is necessary to perform a long-time integration. Figure 8c,d show the integration results of the GRT and GRFT, respectively. It is obvious that neither coherent integration nor noncoherent integration yield significant "spikes" in the cases in which the target echo is partially coherent. Figure 8e shows the integration result of the proposed method. The initial coherent integration segment is set to be $t_{min} = 0.0026$ s; that is, $k_{min} = 8$. After iterating four times, the system obtains the optimal output. The sought after coherent integration segment time is 0.04096 s. It is evident that the peak clearly appears in the correct motion of the target. Figure 8f shows the integration result of MTD-GRT method, and the coherent integration segment time is set to 0.04096 s. One can see that there is no "peak". Figure 8g–j show the integration results of GRT, GRFT, the proposed algorithm, and MTD-GRT with the simulated data. The parameters of the simulated data are the same as those of the measured data. The initial coherent integration segment of the proposed algorithm is also set to be $t_{min} = 0.0026$ s. In addition, the iterating time is also four to gain the optimal output. The integration results from Figure 8g–j are consistent with those from Figure 8c–f.
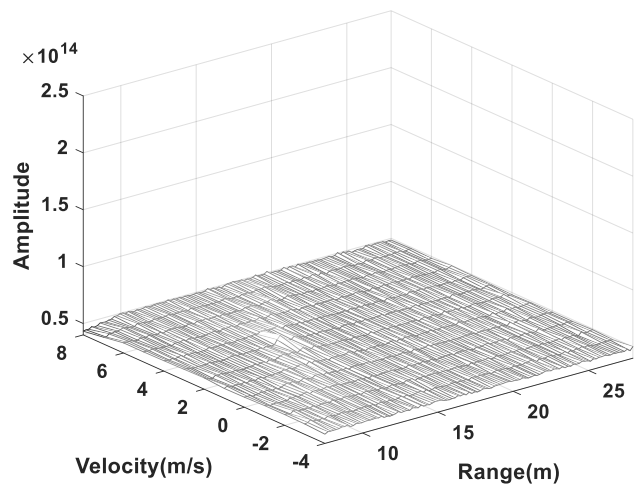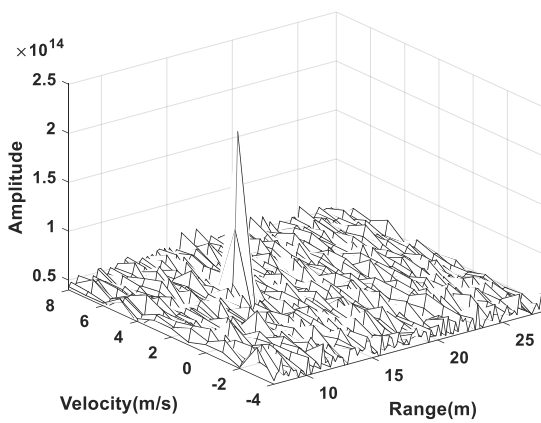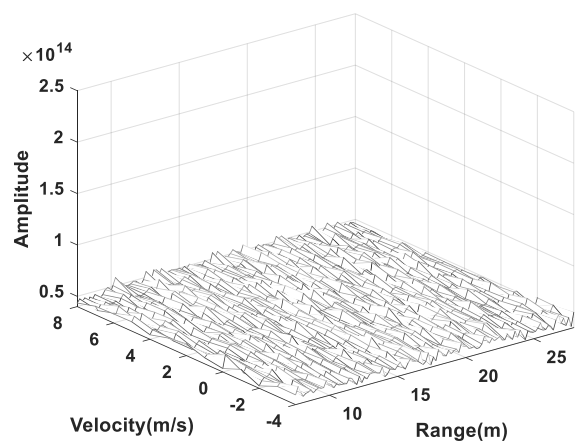
(**a**)
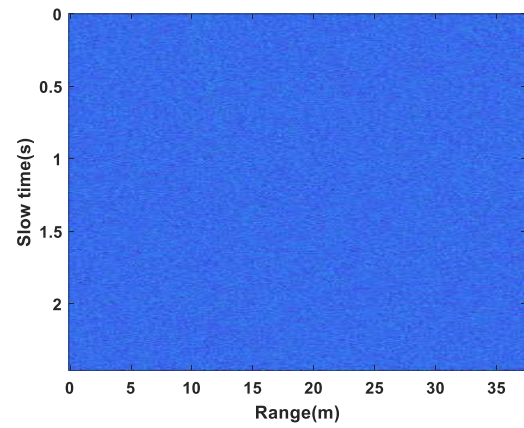
(**b**)

(**c**)

(**d**)

(**e**)

(**f**)

Figure 8. *Cont.*

(**g**)

(**h**)

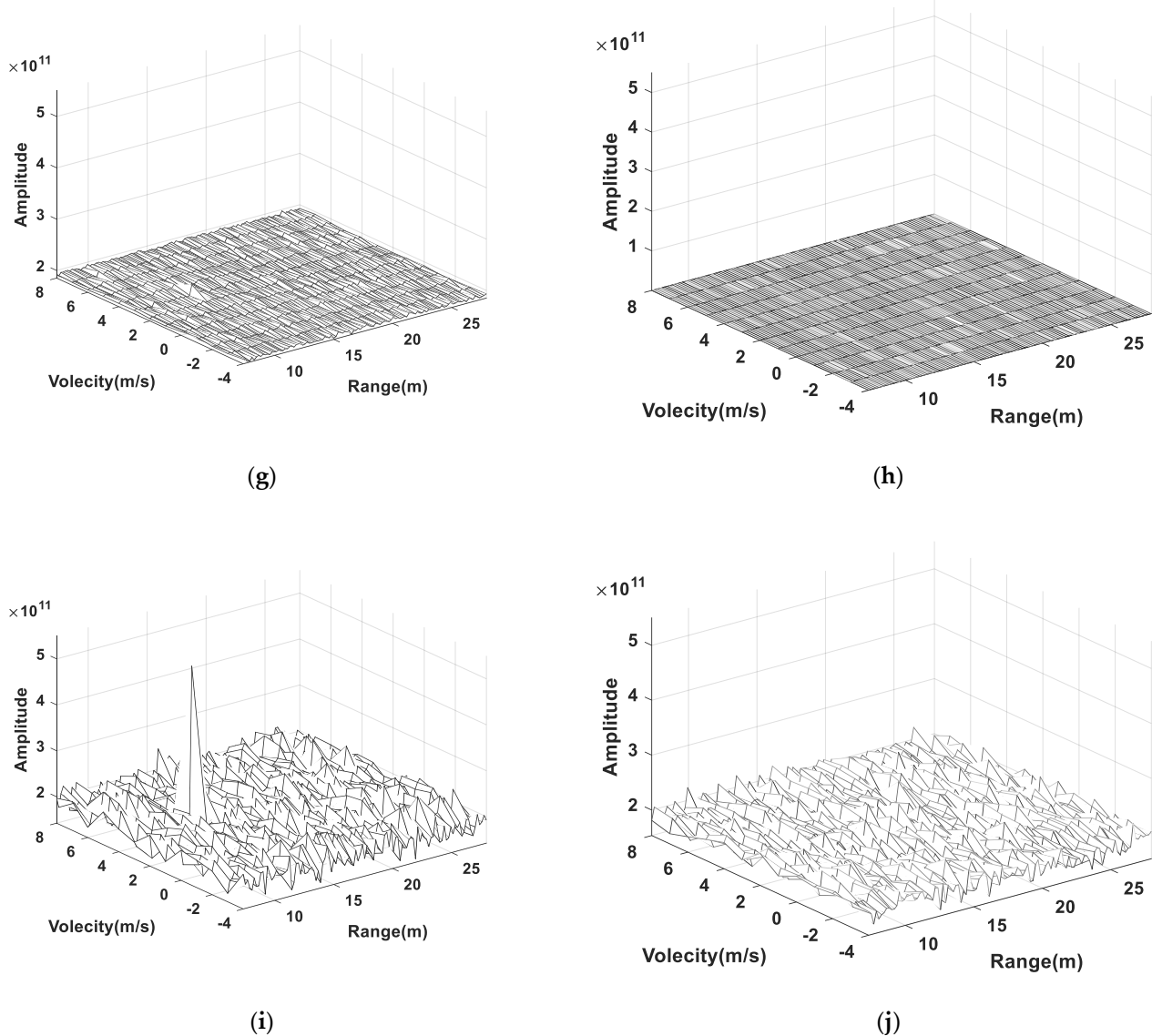
(**i**)

(**j**)
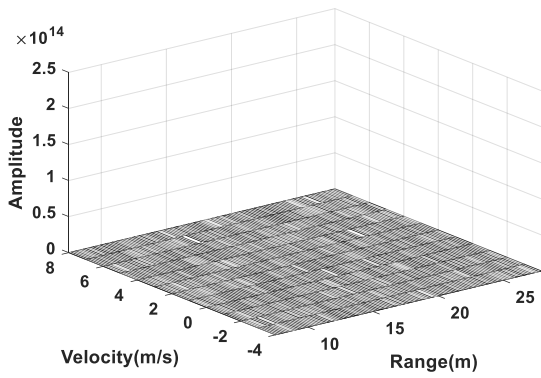
Figure 8. Processing results: (**a**) The detection scenario; (**b**) Measured data result after dechirping; (**c**) Measured data integration result via GRT; (**d**) Measured data integration result via GRFT; (**e**) Measured data integration result via the proposed method; (**f**) Measured data integration result via MTD-GRT; (**g**) Simulated data integration result via GRT; (**h**) Simulated data integration result via GRFT; (**i**) Simulated data integration result via the proposed method; (**j**) Simulated data integration result via MTD-GRT.

5. Conclusions

This study presents a brand-new hybrid integration method for partially fluctuating targets. First, the GRFT method is used for the coherent integration within the coherent integration segment, and then the GRT method is used for the noncoherent integration between coherent integration segments. To yield the optimal coherent integration gain, this study proposes the optimal coherent integration segment search method. The proposed method offers the following benefits: (1) it is suitable for low SNRs, (2) it can be generalized to multitarget situations, and (3) it is applicable to arbitrary fluctuating targets. Compared with noncoherent integration, coherent integration, the MTD-GRT, and other methods, the proposed method offers optimal detection performance and contributes to optimal coherent integration segmentation. Since the results of the simulation experiment and the results from the measured data processing show the highest gain in the partially coherent

echo and up to 8 dB higher than other methods in high-speed situations, thus verifying the effectiveness of the proposed method, the proposed method has bright prospects. However, each coin has two sides. The high degree of computational complexity for the global search of the proposed algorithm should be further decreased in our future work.

Author Contributions: Z.Z. and N.L. were involved in the computational framework, conceptualization, methodology, data analysis, results interpretation, and paper writing; Y.H. simulated the experiments and processed the measured data; S.Z. was involved in the methodology; L.Z. performed the general supervision of the study and provided solutions to any problems that arose. All authors have read and agreed to the published version of the manuscript.

Data Availability Statement: Not applicable.

Conflicts of Interest: The authors declare no conflict of interest.

Abbreviations

s	Pulse compressed signal.
m	Slow-time sampling point number.
n	in-pulse fast-time sampling point number.
c	Speed of light.
B	Signal bandwidth.
ρ_r	Range resolution.
λ	Wavelength.
f_c	Carrier frequency.
R	Radial range of the target.
σ	Complex backscattering coefficient.
N	Noise.
R_σ	Correlation function.
T_r	Radar pulse repetition cycle.
T_{CI}	Echo decorrelation time.
h	Phase compensation function.
K	Totally integrated pulses.
K_{CI}	Coherent integration segments.
k_{CI}	Number of pulses in each coherent integration segment.
g_{CI}	Coherent integration result in coherent integration segment.
g_{HI}	Hybrid integration result.
$t_{\min}$	The minimum coherent time.
$k_{\min}$	Minimum number in coherent integration segment.
V_T	Detection threshold.
C_{H1}	Covariance matrix of the observation matrix.
C_S	Covariance matrix of the target echo signal.
A	Integration matrix.
S	Matrix of echo signal.
$g_{CI}^{(i)}$	Coherent integration result via level-i data.
$g_{HI}^{(i)}$	Hybrid integration result via level-i data.
$(\cdot)^H$	Hermitian transpose operation.
$\lceil \cdot \rceil$	Round-up-to-integer operation.

Appendix A

Under the H1 hypothesis, noise and target information exist at the same time, and the covariance matrix of the observation matrix can be expressed as:

$$\begin{aligned} \boldsymbol{C}_{H1} &= \mathrm{E}\left[\boldsymbol{SS}^H\right] \\ &= \boldsymbol{C}_S + \boldsymbol{I} \end{aligned} \tag{A1}$$

where $\boldsymbol{S} = \begin{bmatrix} s(1,1) & s(1,2) & \cdots & s(1,m) \\ s(2,1) & s(2,2) & \cdots & s(2,m) \\ \vdots & \vdots & \ddots & \vdots \\ s(n,1) & s(n,2) & \cdots & s(n,m) \end{bmatrix}$, and $\boldsymbol{C}_S$ is the covariance matrix of the target echo signal. Since the noise is white Gaussian noise, its covariance matrix should be $\boldsymbol{I}$. $\boldsymbol{C}_{H1}$ is a positive definite matrix, so it can be expressed as [50]:

$$\boldsymbol{C}_{H1} = \boldsymbol{LL}^H \tag{A2}$$

where $\boldsymbol{L}$ is a $K \times K$-dimension invertible matrix.

Hybrid integration can also be expressed in matrix form:

$$\varpi_{H1} = \boldsymbol{S}^H \boldsymbol{AS}$$

where $\boldsymbol{A} = \begin{bmatrix} \boldsymbol{A}_{CI} & & & \\ & \boldsymbol{A}_{CI} & & \\ & & \ddots & \\ & & & \boldsymbol{A}_{CI} \end{bmatrix}$ is an integration matrix and $\boldsymbol{A}_{CI} = \begin{bmatrix} 1 & 1 & \cdots & 1 \\ 1 & 1 & \cdots & 1 \\ \vdots & \vdots & \ddots & \vdots \\ 1 & 1 & \cdots & 1 \end{bmatrix}$ is

a $k_{CI} \times k_{CI}$-dimension all-1 matrix. A linear transform $\boldsymbol{V}_K = \boldsymbol{L}^{-1}\boldsymbol{S}$ is defined, such that the original hybrid integration result can be expressed as:

$$\varpi_{H1} = \boldsymbol{V}_K^H \boldsymbol{P} \boldsymbol{V}_K \tag{A3}$$

where $\boldsymbol{P} = \boldsymbol{L}^H \boldsymbol{AL}$ is a Hermitian Matrix, when $\boldsymbol{V}_K$ is still a Gaussian process [51].

Hence, the similar diagonalizable matrix of $\boldsymbol{P}$ is:

$$\boldsymbol{U}^H \boldsymbol{P} \boldsymbol{U} = diag(\lambda_1, \lambda_2, \cdots, \lambda_K) \tag{A4}$$

where $\boldsymbol{U}$ is a unitary matrix, and $\lambda_i, i = 1, 2, \cdots, K$ is the eigenvalue of $\boldsymbol{P}$. Since the rank of $\boldsymbol{A}$ is the same as that of $\boldsymbol{P}$, then $\lambda_i = 0, i = K_{CI} + 1, \cdots, K$. Another linear transform $\boldsymbol{Y} = \boldsymbol{U}^H \boldsymbol{V}$ is defined; then, the hybrid integration result can be further expressed as:

$$\varpi_{H1} = \boldsymbol{Y}^H \boldsymbol{D} \boldsymbol{Y} = \sum_{i=1}^{K_{CI}} \lambda_i |y_i|^2 = \frac{1}{2}\sum_{i=1}^{K_{CI}} \lambda_i \left(2|y_i|^2\right) \tag{A5}$$

where $\boldsymbol{D} = \boldsymbol{U}^H \boldsymbol{P} \boldsymbol{U} = diag\left(\lambda_1, \lambda_2, \cdots, \lambda_{K_{CI}}, 0, \cdots, 0\right)$ is a diagonal matrix; $\boldsymbol{Y}$ is a Gaussian process; y_i is an element in $\boldsymbol{Y}$, namely, an independent and identically distributed Gaussian variable; then, $2|y_i|^2$ is a Chi square variable with two degrees of freedom. Then, ϖ_{H1} should obey the Gamma distribution [52], and its probability density function can be expressed as:

$$p_{\varpi H1}(x; \alpha_1, \beta_1 | H_1) = f_{\Gamma}(x; \alpha_1, \beta_1/2) \tag{A6}$$

where $\alpha_1 = \left(\sum\limits_{i=1}^{K_{CI}} \lambda_i\right)^2 / \sum\limits_{i=1}^{K_{CI}} \lambda_i^2, \beta_1 = 2\sum\limits_{i=1}^{K_{CI}} \lambda_i^2 / \sum\limits_{i=1}^{K_{CI}} \lambda_i, \ f_{\Gamma}(x; \alpha, \beta) = \frac{\beta^\alpha x^{\alpha-1} e^{-\beta x}}{\Gamma(\alpha)},$ $\Gamma(\alpha) = \int_0^\infty x^{\alpha-1} e^{-x} dx.$

Then, the detection probability can be expressed as:

$$P_d = \int_{V_T}^{+\infty} p_{\varpi H1}(x; \alpha_1, \beta_1 | H_1) dx = F(V_T; \alpha_1, \beta_1/2) \tag{A7}$$

where $F(x; \alpha, \beta) = \frac{\eta(\alpha, \beta x)}{\Gamma(\alpha)}$ is the Gamma distribution function and V_T is the detection threshold.

There is only noise under the H0 hypothesis; similar to the above-noted deviation, the following is achieved through the similar diagonalization of matrix $\boldsymbol{P}$:

$$\boldsymbol{U}^H \boldsymbol{P} \boldsymbol{U} = diag(\varepsilon_1, \varepsilon_2, \cdots, \varepsilon_K, 0, \cdots, 0) \tag{A8}$$

where $\varepsilon_i = k_{CI}, i = 1, 2, \cdots, K_{CI}$. Then, the hybrid integration result can be simplified as:

$$\varpi_{H0} = k_{CI} \sum_{i=1}^{K_{CI}} |y_i|^2 \tag{A9}$$

The false alarm probability of the hybrid integration process can be expressed as:

$$P_{fa} = \int_{V_T}^{+\infty} p_{H0}(x | H0) dx = Q_{\chi^2_{2K_{CI}}}(2V_T / k_{CI}) \tag{A10}$$

where $p_{H0}(x|H0) = \int_{V_T}^{+\infty} \frac{2}{k_{CI}} p_{\chi^2_{2K_{CI}}}\left(\frac{2}{k_{CI}} x\right)$ is the probability density function of the hybrid integration process, and $p_{\chi^2_{2K_{CI}}}(x)$ represents the probability density function of the variable with a Chi-square distribution.

The detection threshold can also be expressed as:

$$V_T = \frac{k_{CI}}{2} Q_{\chi^2_{2K_{CI}}}^{-1}\left(P_{fa}\right) \tag{A11}$$

where $Q_{\chi^2_{2K_{CI}}}^{-1}(\cdot)$ represents the inverse function of the right tail probability of the Chi-square distribution variable.

References

1. Xu, J.; Peng, Y.; Xia, X.; Farina, A. Focus-before-detection radar signal processing: Part I—Challenges and methods. *IEEE Aerosp. Electron. Syst. Mag.* **2017**, *32*, 48–59. [CrossRef]
2. Huang, X.; Zhang, L.; Zhang, J.; Li, S. Efficient angular chirp-Fourier transform and its application to high-speed target detection. *Signal Process.* **2019**, *164*, 234–248. [CrossRef]
3. Huang, X.; Zhang, L.; Li, S.; Zhao, Y. Radar highspeed small target detection based on keystone transform and linear canonical transform. *Digit. Signal Process.* **2018**, *82*, 203–215. [CrossRef]
4. Tao, R.; Zhang, N.; Wang, Y. Analysing and compensating the effects of range and Doppler frequency migrations in linear frequency modulation pulse compression radar. *IET Radar Sonar Navig.* **2010**, *5*, 12–22. [CrossRef]
5. Xu, Z.; Baker, C.J.; Pooni, S. Range and Doppler cell migration in wideband automotive radar. *IEEE Trans. Veh. Technol.* **2019**, *68*, 5527–5536. [CrossRef]
6. Huang, X.; Tang, S.; Zhang, L.; Li, S.; Lin, C.; Liu, N. Low-observable maneuvering target detection based on Radon-advanced discrete chirp Fourier transform. In Proceedings of the IEEE Radar Conference, Seattle, WA, USA, 8–12 May 2017; pp. 0735–0738.
7. Richards, M.A.; Scheer, J.A.; Holm, W.A. *Principles of Modern Radar: Basic Principles*; Scitech: New York, NY, USA, 2010; pp. 259–261.
8. Cui, G.; Demaio, A.; Piezzo, M. Performance prediction of the incoherent radar detector for correlated generalized swerling-chi fluctuating targets. *IEEE Trans. Aerosp. Electron. Syst.* **2012**, *49*, 356–368. [CrossRef]
9. Swerling, P. Probability of detection for fluctuating targets. *IRE Trans. Inf. Theory* **1960**, *6*, 269–308. [CrossRef]
10. Swerling, P. Radar probability of detection for some additional fluctuating target cases. *IEEE Trans. Aerosp. Electron. Syst.* **1997**, *33*, 698–709. [CrossRef]
11. Maio, A.D.; Farina, A.; Foglia, G. Target fluctuation models and their application to radar performance prediction. *IEE Proc. Radar Sonar Navig.* **2004**, *151*, 261–270. [CrossRef]

12.　Cui, G.; Maio, A.D.; Carotenuto, V. Performance prediction of the incoherent detector for a weibull fluctuating target. *IEEE Trans. Aerosp. Electron. Syst.* **2014**, *50*, 2176–2184. [CrossRef]

13.　He, Z.; Yang, Y.; Chen, W. A hybrid integration method for moving target detection with GNSS-based passive radar. *IEEE J. Sel. Top. Appl. Earth Obs. Remote Sens.* **2020**, *14*, 1184–1193. [CrossRef]

14.　Lin, H.; Zeng, C.; Zhang, H.; Jiang, G. Motion parameter estimation of high-speed manoeuvering targets based on hybrid integration and synchrosqueezing transform. *IET Radar Sonar Navig.* **2022**, *16*, 852–868. [CrossRef]

15.　Carlson, B.D.; Evans, E.D.; Wilson, S.L. Search radar detection and track with the Hough transform. I. System concept. *IEEE Trans. Aerosp. Electron. Syst.* **1994**, *30*, 102–108. [CrossRef]

16.　Carlson, B.D.; Evans, E.D.; Wilson, S.L. Search radar detection and track with the Hough transform. II. Detection statistics. *IEEE Trans. Aerosp. Electron. Syst.* **1994**, *30*, 109–115. [CrossRef]

17.　Carlson, B.D.; Evans, E.D.; Wilson, S.L. Search radar detection and track with the Hough transform. III. Detection performance with binary integration. *IEEE Trans. Aerosp. Electron. Syst.* **1994**, *30*, 116–125. [CrossRef]

18.　Moqiseh, A.; Nayebi, M.M. Combinational Hough transform for surveillance radar target detection in a 3-D data map. In Proceedings of the IEEE Radar Conference, Rome, Italy, 26–30 May 2008; pp. 1–6.

19.　Moyer, L.R.; Spak, J.; Lamanna, P. A multi-dimensional Hough transform-based track-before-detect technique for detecting weak targets in strong clutter backgrounds. *IEEE Trans. Aerosp. Electron. Syst.* **2011**, *47*, 3062–3068. [CrossRef]

20.　Orlando, D.; Venturino, L.; Lops, M.; Ricci, G. Space-time adaptive algorithms for track-before-detect in clutter environments. In Proceedings of the IEEE International Radar Conference, Bordeaux, France, 12–16 October 2009; pp. 1–6.

21.　Jiang, H.; Yi, W.; Cui, G.; Kong, L.; Yang, X. Track-before-detect strategies for range distribution target detection in compound-Gaussian clutter. *Signal Process.* **2016**, *120*, 462–467. [CrossRef]

22.　Orlando, D.; Venturino, L.; Lops, M.; Ricci, G. Track-before-detect strategies for step radars. *IEEE Trans. Signal Process.* **2010**, *58*, 933–938. [CrossRef]

23.　Yi, W.; Morelande, M.R.; Kong, L.; Yang, J. An efficient multi-frame track-before-detect algorithm for multi-target tracking. *IEEE J. Sel. Top. Signal Process.* **2013**, *7*, 421–434. [CrossRef]

24.　Yi, W.; Morelande, M.R.; Kong, L.; Yang, J. A computationally efficient particle filter for multi-target tracking using an independence approximation. *IEEE Trans. Signal Process.* **2013**, *61*, 843–856. [CrossRef]

25.　Zhang, S.; Zeng, T.; Long, T.; Yuan, H. Dim target detection based on keystone transform. In Proceedings of the IEEE International Radar Conference, Arlington, VA, USA, 9–12 May 2005; pp. 889–894.

26.　Pignol, F.; Colone, F.; Martelli, T. Lagrange-polynomial-interpolation-based keystone transform for a passive radar. *IEEE Trans. Aerosp. Electron. Syst.* **2018**, *54*, 1151–1167. [CrossRef]

27.　Xu, J.; Yan, L.; Zhou, X.; Long, T.; Xia, X.; Wang, Y.; Farina, A. Adaptive Radon-Fourier transform for weak radar target detection. *IEEE Trans. Aerosp. Electron. Syst.* **2018**, *54*, 1641–1663. [CrossRef]

28.　Rao, X.; Zhong, T.; Tao, H.; Xie, J.; Su, J. Improved axis rotation MTD algorithm and its analysis. *Multidimens. Syst. Signal Process.* **2019**, *30*, 595–603. [CrossRef]

29.　Zheng, J.; Su, T.; Zhu, W.; He, X.; Liu, Q. Radar high-speed target detection based on the scaled inverse Fourier transform. *IEEE J. Sel. Top. Appl. Earth Obs. Remote Sens.* **2015**, *8*, 1108–1119. [CrossRef]

30.　Zheng, J.; Su, T.; Liu, H.; Liao, G.; Liu, Z.; Liu, Q. Radar high-speed target detection based on the frequency-domain Deramp-Keystone transform. *IEEE J. Sel. Top. Appl. Earth Obs. Remote Sens.* **2016**, *9*, 285–294. [CrossRef]

31.　Su, J.; Xing, M.; Wang, G.; Bao, Z. High-speed multi-target detection with narrowband radar. *IET Radar Sonar Navig.* **2010**, *4*, 595–603. [CrossRef]

32.　Li, X.; Cui, G.; Yi, W.; Kong, L. Maneuvering target detection based on keystone transform and Lv's distribution. *IET Radar Sonar Navig.* **2016**, *10*, 1234–1242. [CrossRef]

33.　Fang, X.; Cao, Z.; Min, R.; Pi, Y. Radar maneuvering target detection based on two steps scaling and fractional Fourier transform. *Signal Process.* **2018**, *155*, 1–13. [CrossRef]

34.　Rao, X.; Tao, H.; Xie, J.; Su, J.; Li, W. Long-time coherent integration detection of weak manoeuvring target via integration algorithm, improved axis rotation discrete chirp-Fourier transform. *IET Radar Sonar Navig.* **2015**, *9*, 917–926. [CrossRef]

35.　Chen, S.; Luo, F.; Zhang, L.; Hu, C.; Chen, S. Coherent integration detection method for maneuvering target based on dynamic programming. *Int. J. Electron. Commun.* **2017**, *73*, 46–49. [CrossRef]

36.　Zhao, L.; Tao, H.; Chen, W.; Song, D. Maneuvering target detection based on subspace subaperture joint coherent integration. *Remote Sens.* **2021**, *13*, 1948. [CrossRef]

37.　Xu, J.; Xia, X.; Peng, S.; Yu, J.; Qian, L. Radar maneuvering target motion estimation based on generalized Radon-Fourier transform. *IEEE Trans. Signal Process.* **2012**, *60*, 6190–6201.

38.　Xia, W.; Zhou, Y.; Jin, X.; Zhou, J. A fast algorithm of generalized Radon-Fourier transform for weak maneuvering target detection. *Int. J. Antennas Propag.* **2016**, *2016*, 4315616. [CrossRef]

39.　Li, X.; Cui, G.; Yi, W.; Kong, L. Radar maneuvering target detection and motion parameter estimation based on TRT-SGRFT. *Signal Process.* **2017**, *133*, 107–116. [CrossRef]

40.　Wang, C.; Zheng, J.; Jiu, B.; Liu, H.; Shi, Y. Deep neural network-aided coherent integration method for maneuvering target detection. *Signal Process.* **2021**, *182*, 107966. [CrossRef]

41. Achim, A.; Buxton, B.; Tzagkarakis, G.; Tsakalides, P. Compressive sensing for ultrasound RF echoes using a-stable distributions. In Proceedings of the 2010 Annual International Conference of the IEEE Engineering in Medicine and Biology, Buenos Aires, Argentina, 31 August–4 September 2010; pp. 4304–4307.
42. Hosseini, M.S.; Michailovich, O.V. Derivative compressive sampling with application to phase unwrapping. In Proceedings of the 2009 17th European Signal Processing Conference, Glasgow, UK, 24–28 August 2009; pp. 115–119.
43. Rostami, M.; Cheung, N.M.; Quek, T.Q. Compressed sensing of diffusion fields under heat equation constraint. In Proceedings of the 2013 IEEE International Conference on Acoustics, Vancouver, BC, Canada, 26–31 May 2013; pp. 4271–4274.
44. Pastina, D.; Santi, F.; Pieralice, F.; Bucciarelli, M.; Ma, H.; Tzagkas, D.; Antoniou, M.; Cherniakov, M. Maritime moving target long time integration for GNSS-based passive bistatic radar. *IEEE Trans. Aerosp. Electron. Syst.* **2018**, *54*, 3060–3083. [CrossRef]
45. Zeng, J.; He, Z. Detection of weak target for MIMO radar based on Hough transform. *J. Syst. Eng. Electron.* **2009**, *20*, 76–80.
46. Xu, J.; Zhou, X.; Qian, L.; Xia, X.; Long, T. Hybrid integration for highly maneuvering radar target detection based on generalized Radon-Fourier transform. *IEEE Trans. Aerosp. Electron. Syst.* **2016**, *52*, 2554–2561. [CrossRef]
47. Ding, Z.; You, P.; Qian, L.; Zhou, X.; Liu, S.; Long, T. A subspace hybrid integration method for high-speed and maneuvering target detection. *IEEE Trans. Aerosp. Electron. Syst.* **2019**, *56*, 630–644. [CrossRef]
48. Zhou, X.; Qian, L.; Ding, Z.; Xu, J.; Liu, W.; You, P.; Long, T. Radar detection of moderately fluctuating target based on optimal hybrid integration detector. *IEEE Trans. Aerosp. Electron. Syst.* **2018**, *55*, 2408–2425. [CrossRef]
49. Trunk, G.V. Detection results for scanning radars employing feedback integration. *IEEE Trans. Aerosp. Electron. Syst.* **1970**, *1*, 522–527. [CrossRef]
50. Watkins, A. *Fundamentals of Matrix Computations*; Wiley: New York, NY, USA, 1991; pp. 32–54.
51. Rencher, A.C. *Methods of Multivariate Analysis*; Wiley: New York, NY, USA, 1995; p. 86.
52. Box, G.E.P. Some theorems on quadratic forms applied in the study of analysis of variance problems, I. Effect of inequality of variance in the one-way classification. *Ann. Math. Stat.* **1954**, *25*, 484–498. [CrossRef]